Constituent Effects on the Stress-Strain Behavior of Woven Melt-Infiltrated SiC Composites

G. N. Morscher[1] and J.I. Eldridge[2]

[1]Ohio Aerospace Institute; NASA Glenn Research Center, MS 106-5, Cleveland, OH 44135, USA
[2]NASA Glenn Research Center, MS 106-5, Cleveland, OH 44135, USA

ABSTRACT

The stress-strain behavior of 2D woven SiC fiber reinforced, melt-infiltrated SiC matrix composites with BN interphases were studied for composites fabricated with different fiber tow ends per unit length, different composite thickness, and different numbers of plies. In general, the stress-strain behavior, i.e. the "knee" in the curve and the final slope of the stress-strain curve, was controlled by the volume fraction of fibers. Some of the composites exhibited debonding and sliding in between the interphase and the matrix rather than the more common debonding and sliding interface between the fiber and the interphase. Composites that exhibited this "outside debonding" interface, in general, had lower elastic moduli and higher ultimate strains as well as longer pull-out lengths compared to the "inside debonding" interface composites. Stress-strain curves were modeled where matrix crack formation as a function of stress was approximated from the acoustic emission activity and the measured crack density from the failed specimens. Interfacial shear strength measurements from individual fiber push-in tests were in good agreement with the interfacial shear strength values used to model the stress-strain curves.

KEYWORDS

Ceramic matrix composites, Stress-strain behavior, Acoustic Emission

INTRODUCTION

Woven SiC fiber reinforced, SiC matrix composites are prime candidate materials for a high-speed civil aircraft combustor liner [1,2] as well as other high temperature engine components. A considerable amount of composite development has occurred in order to improve the performance of this material system including evaluating different fiber types, interphases, and matrices. For the reference 2 application, a composite system consisting of a Sylramic® (SYL) fiber (Dow Coming, Midland, MI), a BN interphase and a melt-infiltrated (MI) matrix was down-selected based on this system's superior strength, creep resistance, and thermal conductivity properties in comparison to other SiC/SiC systems (e.g. chemically vapor infiltrated SiC matrix). More recently, a further improvement to the SYL fiber has been developed via elevated temperature treatment in nitrogen containing atmospheres that results in an in situ-BN coating on the Sylramic® fiber [3,4] (referred to here as SYL-iBN). Composites processed with these treated fibers resulted in higher ultimate strengths and improved creep resistance over composites processed with as-produced SYL. However, to date, this latest improved composite has only been fabricated on a small scale.

In order for the SYL/MI-SiC matrix composite system to further mature and be used by designers, the stress-strain response of these materials needs to be well understood and modeled for a range of constituent volume fractions and specimen sizes. For example, components will vary in thickness, curvature, etc. This will require varying numbers of woven fiber plies in specific locations or perhaps different fiber architectures. The

most critical aspect of the stress-strain behavior of these types of composites is not necessarily the ultimate strength properties. Rather, the "knee" in the stress-strain curve, due to the formation of bridged matrix cracks may be more important. For example, the formation of through-thickness matrix cracks usually denotes the stress above which time-dependent strength degradation occurs at intermediate temperatures due to the oxidation of the fiber, interphase and matrix [5-7]. The purpose of this paper will be to compare and model the effect of varying fiber volume fraction on the stress-strain behavior for MI matrix composites using composites with different 2D woven fiber architectures, i.e., varying the numbers of fiber-tows per unit length, the number of plies, and the thickness of the composite specimens.

EXPERIMENTAL

Unload-reload tensile hysteresis tests were performed on over 20 different composite specimens that varied in fiber tow ends per unit length, number of plies, composite thickness or fiber type (SYL or SYL-iBN). Three different vintages of composites were tested in this study. The oldest vintage composites were from the early years of NASA's Enabling Propulsion Materials program [1] and were processed by Carborundum Corporation (Niagara Falls, NY). The next oldest vintage composites were from the latter years of the EPM program and were processed by Honeywell Advanced Composites (Newark, DE.) [2]. The newest vintage composites were processed under NASA's Ultra Efficient Engine Technology (UEET) program and were also fabricated by Honeywell Advanced Composites. The first two vintages consisted of only two different weaves, the same number of plies (8), and similar composite thicknesses (~ 2 mm). Whereas the latter vintage varied fiber tow ends per unit length, composite thickness, and number of plies by nearly a factor of two. This resulted in composite specimens that varied by a factor of two in fiber volume fraction in the loading direction. Table I lists the constituent variations for the composites tested.

TABLE 1
VARIATION IN PROCESSING PARAMETERS FOR DIFFERENT VINTAGE COMPOSITES

Vintage	Variation in Fiber* Tow Ends per Inch	Variation in Number of Five Harness Satin Plies	Variation in Composite Thickness, mm	Variation in Volume Fraction of Fibers in Loading Direction
1	18 or 22	8	2 to 2.3	0.17 to 0.2
2	18 or 22	8	2 to 2.3	0.17 to 0.2
3	12.5, 18, 20, or 22	4, 6, or 8	1.4 to 2.3	0.13 to 0.25

* Each fiber tow consisted of 800 fibers. The average fiber diameter was 10 μm.

Composite processing entails first stacking of the balanced five-harness pieces of cloth of SYL or SYL-iBN fiber, a BN interphase layer deposition (~ 0.5 μm) via chemical vapor infiltration (CVI), a SiC layer deposition via CVI, SiC particulate infiltration via slurry-infiltration, and finally, liquid Si infiltration [1-2].

The tensile tests were performed on specimens with a contoured gage section (dog-bone) using a universal-testing machine (Instron Model 8562, Instron, Ltd, Canton Mass.) with an electromechanical actuator. Glass fiber reinforced epoxy tabs were mounted on both sides of the specimen in the grip regions and the specimens were gripped with rigidly mounted hydraulically actuated wedge grips. A clip on strain gage, with a range of 2.5% strain over 25.4 mm gage length was used to measure the deformation of the gage section.

Modal acoustic emission (AE) was monitored during the tensile tests with two wide-band, 50 kHz to 2.0 MHz, high fidelity sensors placed just outside the tapered region of the dog-bone specimen. Vacuum grease was used as a couplant and mechanical clips were used to mount the sensors to the specimen. The AE waveforms were recorded and digitized using a 4-channel, Fracture Wave Detector (FWD) produced by Digital Wave Corporation (Englewood, CO). The load and strain were also recorded with the FWD. After the tensile test, the AE data was filtered using the location software from the FWD manufacturer in order to separate out the AE that occurred outside of the gage section. For more information on the AE procedure and analysis, see references 8 and 9.

Fracture surfaces were observed with a field emission scanning electron microscope (Hitachi S-4700, Tokyo, Japan). Since the compressive stress in the matrix closes the matrix cracks, to measure crack density, sections of the tested tensile specimens in the gage section at least 10 mm long were polished and then plasma

(CF$_4$) etched at 500 W for 30 minutes. The etchant reacts with the free Si in the matrix, removing much of it, making it impossible to observe cracks in the MI part of the matrix. Matrix cracks can only be observed in the dense CVI SiC layer between the BN and the MI matrix.

Push-in tests were performed on a few specimens from sections of the composite that were in the mechanical grips in order to measure the interfacial shear stress, τ, of the sliding interface. Specimens were cut and polished to a thickness of ~ 1mm. The procedure for the push-in technique, the apparatus used, and the analysis can be found in reference 10. The average τ was determined from at least 20 different fibers for each specimen.
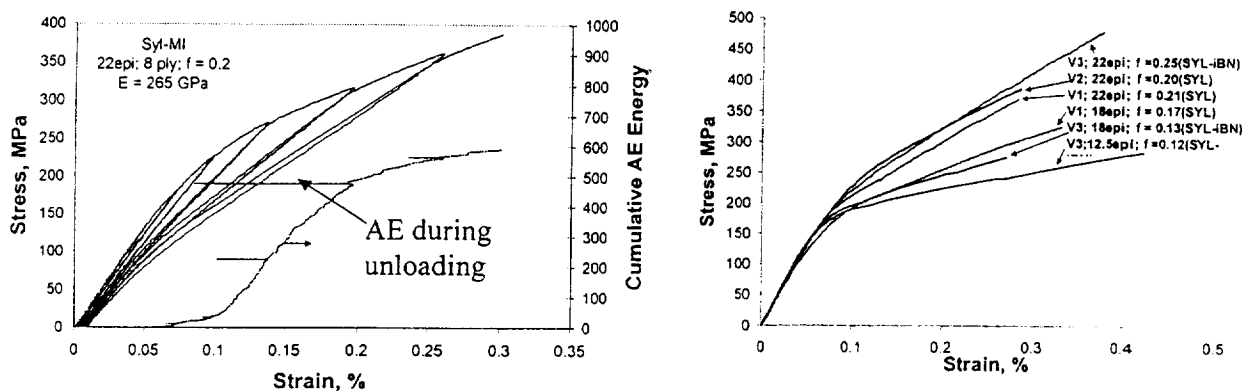
RESULTS AND DISCUSSION

Figure 1: (a) Typical unload-reload stress-strain curve and cumulative AE energy for a vintage 2 SYL-MI composite. (b) Stress-strain curves (hysteresis loops removed) for composites with a variety of fiber volume fractions, f, in the loading direction and fiber tow ends per unit length (ends per inch) from all three composite vintages.

A typical hysteresis tensile stress-strain curve for a SYL-MI composite is shown in Figure 1a. All Sylramic-MI SiC composites stiffen during unloading due to matrix crack closure presumably due to residual compression in the matrix [11]. The AE activity is also plotted in Figure 1 in the form of cumulative AE energy. It was found in earlier studies that cumulative energy was the best AE parameter to correlate AE activity with matrix cracking [8-9]. Matrix crack formation and growth occurs in a similar fashion to that described in other studies [12-14] for 2D composites. At low stresses, microcracks form in the 90° bundles and/or large matrix only regions (tunnel cracks). With increasing stress these cracks grow and become through-thickness matrix cracks and new cracks form. At higher stresses, the formation of matrix cracks diminishes and may cease altogether; however, for SYL-MI composites, matrix crack saturation was not always achieved.

Figure 1b shows a number of stress-strain curves with different fiber volume fractions. The elastic moduli were all similar for the composites in Figure 1b (265 to 280 GPa); however, elastic moduli as low as 220 GPa have been recorded. In general, an increase in fiber volume fraction results in an increase in the "knee" of the stress-strain curve as well as an increase in the slope of the stress-strain curve after the "knee" in the curve, as would be expected. Also, the SYL-iBN reinforced composites usually had higher ultimate strengths and strains for the same volume fraction/architecture when compared to SYL reinforced composites as was found in the other study [4]. The fracture surfaces of most specimens tested were observed using a field emission scanning electron microscope. For specimens corresponding to Figure 1a, it was verified that the fibers pulled-out between the fiber and the interphase (inside debonding) and had relatively short fiber pull-out lengths (Figure 2), typical of SYL-BN composites.

For some of the vintage 3 composites, debonding and sliding occurred between the interphase and the matrix (outside debonding, see Figure 3). For these composites, large pullout-lengths, higher strain to failure (Figure 4a) and lower elastic moduli (Figure 4a) were generally observed. However, some specimens with "outside debonding" had elastic moduli on the order of the "inside debonding" composites of Figure 1a but still had larger strains for a given stress at stresses above the "knee" in the stress-strain curve in comparison to "inside debonding" composites. This was the first time that debonding and sliding had been observed to occur on the outer interface between the interphase and the matrix for SYL reinforced composites. Presumably, this interface
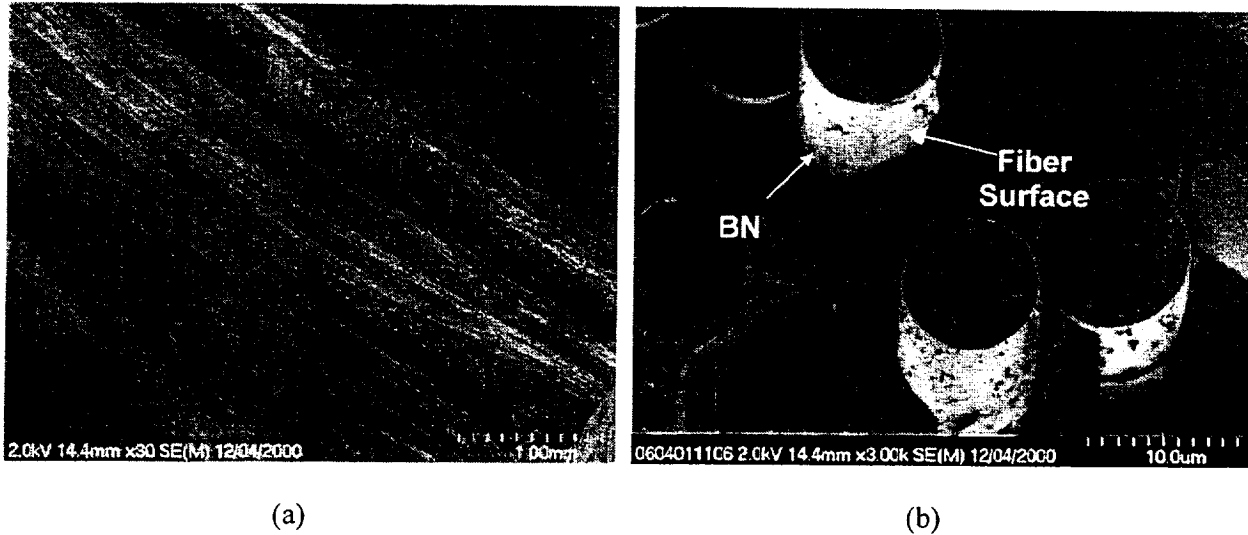

(a)   (b)

Figure 2: Fracture surface from a SYL-iBN composite where the fibers debonded between the fiber and the interphase (inside debonding).

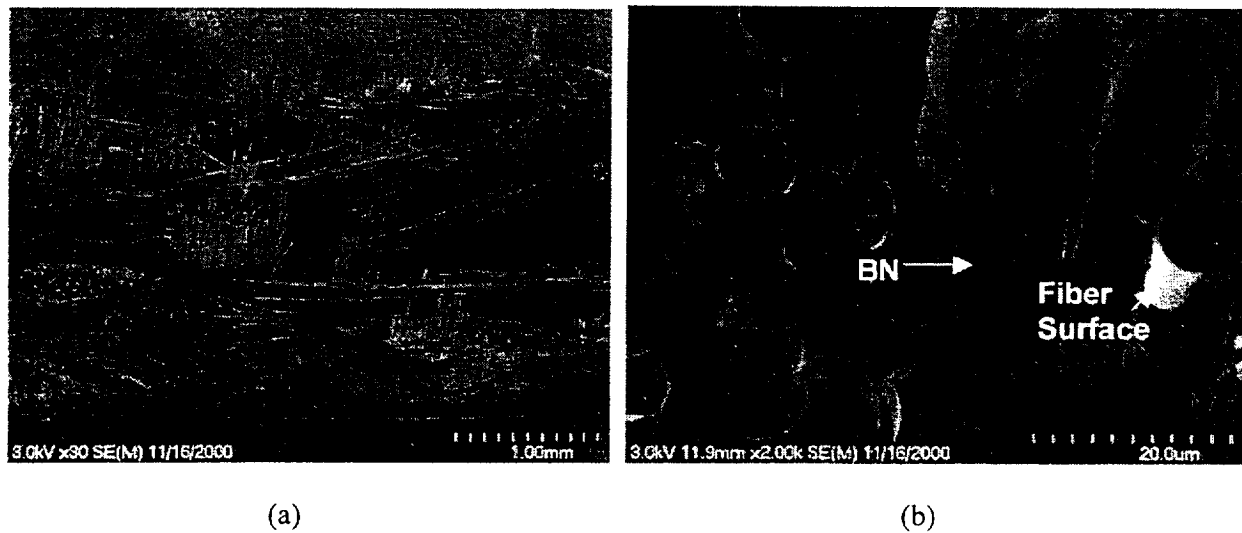(a)   (b)

Figure 3: Fracture surface from a SYL-iBN composite where the fibers debonded between the interphase and the matrix (outside debonding).

was weaker and possibly debonded during cool down of the composite as the residual tension at the interphase increased with decreasing temperature. The residual compressive stress was estimated from intersection of the average slopes of the upper portions of the hysteresis loops (see Figure 1, after Steen [11]). It was found that for "inside debonding" composites, the residual stress was dependent on fiber volume fraction (Figure 4b). Many of the "outside debonding" composites had smaller residual compressive stresses for the same volume fraction compared to the "inside debonding" composites, especially for SYL-iBN composites (Figure 4b).

It was desired to model the stress-strain behavior in order to estimate the interfacial shear stress and to see if the "knee" in the stress-strain curve could effectively be accounted for. However, modeling the stress-strain behavior depends on accurately determining the stress at which matrix cracks will form and the extra displacement associated with the increased load applied to the fibers bridging the matrix crack. This was first done for unidirectional fiber reinforced composites assuming the matrix possessed an infinite Weibull modulus [15]. Later modifications incorporated the effects of residual stress due to thermal expansion mismatches between the fiber and the matrix [16]. However, for SiC/SiC composites, matrix fracture is dependent on the flaw population in the matrix [17]. Therefore, matrix cracking occurs over a range of applied stress. In addition, 2D lay-up or woven composites have been shown to possess different types of matrix cracks that originate either at pores in the matrix, in the 90° plies, or in the 0° plies with increasing stress, at least for CVI SiC matrix composites [12-14].
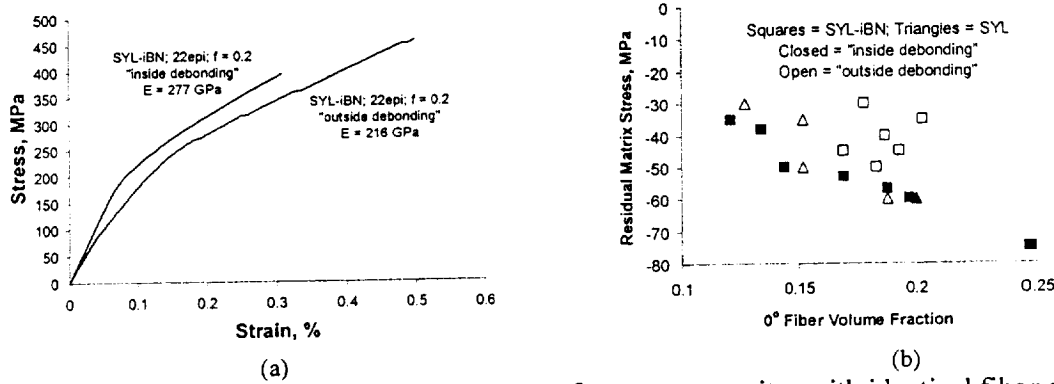

Figure 4: Comparison of (a) stress-strain curves for two composites with identical fiber architectures (hysteresis loops removed) and (b) residual compressive stress in the matrix for composites with "inside debonding" (vintages 2 and 3) and "outside debonding" (vintage 3).

Cumulative AE energy has been related to the number of transverse matrix cracks [9]; however, it only gives the relative amount of cracking. In order to use AE energy for absolute crack densities, the AE energy must be calibrated to a known crack density at a specific stress. This was done for most of the composites after fracture. For composites where crack saturation was believed to occur, crack densities were measured to be 11.0 ± 4.0 and 8.7 ± 0.7 cracks/mm for "inside debonding" and "outside debonding" composites, respectively. However, there was no apparent relation between fiber volume fraction, specimen thickness, or ends per unit length and saturation crack density.

Composite strain was determined in the same fashion as Pryce and Smith [18]. Using the nomenclature of Curtin, et al. [19], composite strain can be modeled for equally spaced cracks:

$$\varepsilon = \sigma/E_c + \alpha\delta(\sigma)\rho_c/E_f \ (\sigma + \sigma_{th}); \qquad \text{for } \rho_c^{-1} > 2\delta \qquad (1)$$

where the first part of the equation corresponds to the elastic strain response of an uncracked composite and the second part of the equation corresponds to the extra strain (displacement) of the fibers at and away from a through-thickness matrix crack dictated by the sliding length:

$$\delta = \alpha \ r \ (\sigma + \sigma_{th}) \ / \ 2\tau \qquad (2)$$

where

$$\alpha = (1-f) \ E_m \ / \ f \ E_c \qquad (3)$$

σ is the applied stress, σ_{th} is the residual (thermal) stress in the matrix (compression is negative), E is the elastic modulus, subscripts m, f and c refer to matrix, fiber, and composite, respectively, ρ_c is the matrix crack density, r is the fiber radius, and τ is the interfacial shear strength. E_c and σ_{th} were determined from the stress strain curves. E_f is 380 GPa and E_m was determined from the rule of mixtures. ρ_c was estimated from the AE energy based on the known crack spacing from the stress-rupture tests. Therefore, the only variable not known was τ which was adjusted in order to best fit the predicted stress strain curve to the experimental stress strain curve. For the case

where the sliding lengths overlap, Ahn and Curtin [20] showed that if the cracks are still equally spaced, the composite strain could then be modeled by:

$$\varepsilon = \sigma / (f\, E_f) + \alpha\, \sigma_{th} / E_f - \alpha\, (\sigma + \sigma_{th}) / [4\, E_f\, \delta(\sigma)\, \rho_c]; \quad \text{for } \rho_c^{-1} < 2\delta \qquad (4)$$

Therefore, for higher applied stress conditions, if $\rho_c^{-1} < 2\delta$ was predicted, equation (4) was used.

Figure 5a to 5d show the room temperature experimental stress-strain curve, the AE activity, and predicted stress-strain curve using the best-fitted τ value and for τ values 20% greater and 20% less than the best-fit value for "outside debonding" and "inside debonding" composites. The ultimate stress was not predicted, the curves were only plotted to the known ultimate strength of the individual specimen. The predicted stress-strain curves are in good agreement with the experimental stress-strain curves. "Outside debonding" composites required lower τ values to model the stress-strain curve: 31 ± 6 MPa for two SYL composite specimens and 15 ± 4 MPa for two SYL-iBN composite specimens. "Inside debonding" composites required higher τ values: 64 ± 1 MPa for two SYL composite specimens and 71 ± 10 for four SYL-iBN composite specimens. Presumably, the lower τ for "outside debonding" composites is due to the smoother sliding interface. Average τ values had been measured for the SYL-iBN "outside debonding" specimen (Fig. 5a), SYL-iBN "inside debonding" specimen (Fig. 5b), and the SYL "inside debonding" specimen (Figure 5d) from push-in tests and were found to be 7 ± 5 MPa, 83 ± 25, and 64 ± 19 MPa, respectively. These values are in very good agreement with the τ values used to model the stress-strain curve for inside debonding composites.

The "knee" in the stress-strain curve was modeled very well using the AE data and final crack spacing to estimate the matrix crack distribution. The only exception was for the SYL "inside debonding" composite (Figure 5d), where the predicted stress-strain curve underestimated the strain at stresses corresponding to the "knee" in the
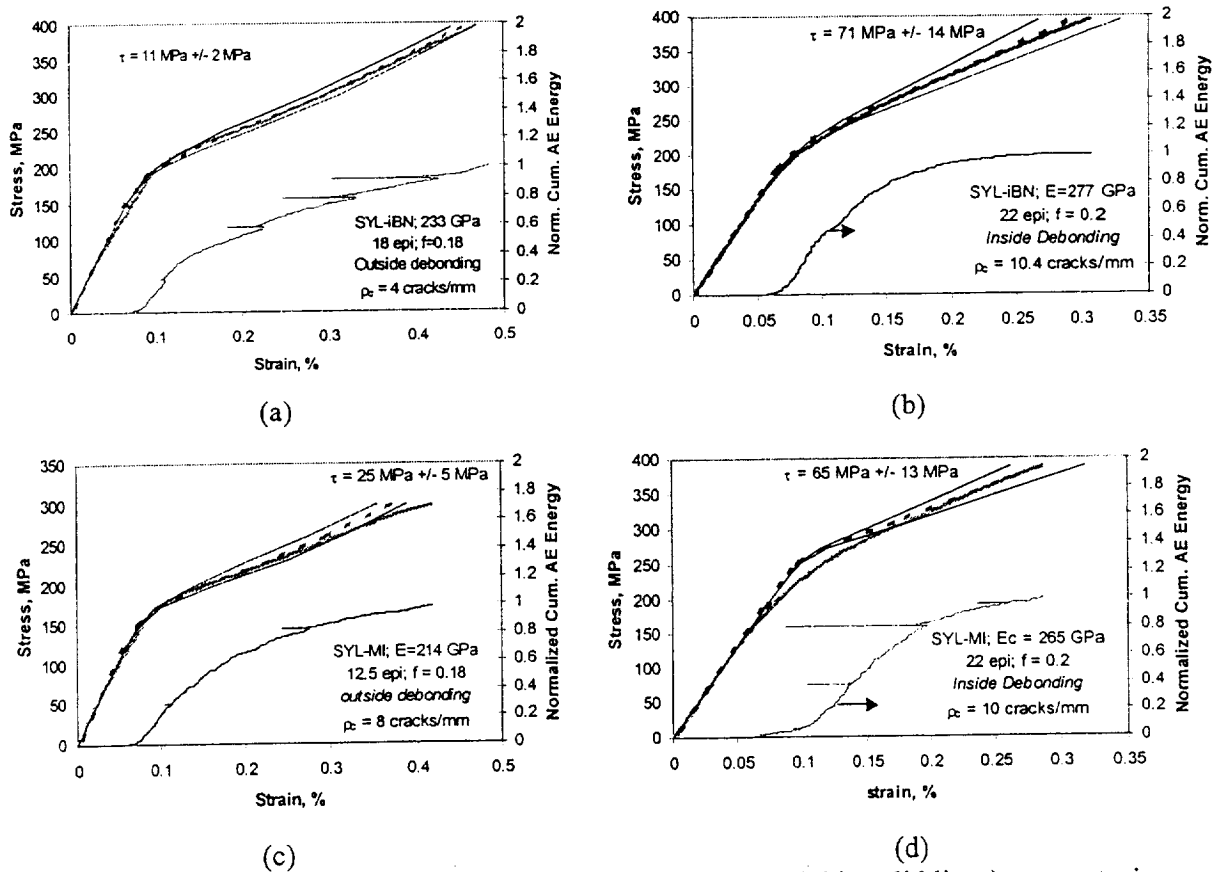

Figure 5: Experimental (thick solid line) and predicted (dashed and thin solid lines) stress-strain curves for an (a) SYL-iBN outside debonding, (b) SYL-iBN inside debonding, (c) SYL outside debonding, and (d) SYL inside debonding composites. Also shown is the normalized cumulative AE energy (AE energy normalized by the maximum cumulative AE energy).

stress-strain curve. The predicted stress-strain behavior for Figure 5d was the worst of all ten specimens modeled. The other SYL "inside debonding" composites was modeled similar to Figure 5b except with a $\tau = 63$ MPa.

CONCLUSIONS

The room temperature stress-strain behavior of Sylramic reinforced melt-infiltrated composites was shown to be most dependent on the volume fraction of fibers in the loading direction for various 2D architectures and composite thickness variations. Some specimens exhibited debonding on the outer interface between the BN interphase and the CVI SiC matrix-layer. This resulted in lower elastic moduli, in general, lower interfacial shear strengths, and higher strains to failure. It is unknown as to the benefits of such behavior at elevated temperature; however, the improvement in composite toughness is obvious. Outside debonding may also aid intermediate temperature properties since the environment would have to react through the interphase layer rather than having direct access to load-bearing fibers. However, interlaminar and high temperature creep/rupture properties still need to be determined in order to ascertain whether or not there is a benefit for this interfacial sliding behavior.

The composite stress-strain curves could be effectively modeled based on the approaches of references 18 and 20. However, this required several parameters to be directly or indirectly determined including the dependence of matrix cracking with stress from AE activity and final crack densities, composite elastic modulus, and matrix residual stress. The approach to best fit the predicted stress-strain curve to the actual data by varying τ provided a way of determining τ that was in very good agreement with measured values.

REFERENCES

1. Johnson, A.M., Bartlett, B.J., and Troha, W.A. (1997). In: *Thirteenth International Symposium on Air Breathing Engines*, pp. 1321-1328. Billig, F.S. (Ed.). American Institute of Aeronautics and Astronautics.
2. Brewer, D. (1999) *Mater. Sci. Eng.*, A261, 284.
3. Yun, H.M. and DiCarlo, J.A. (2000) *Ceram. Eng. Sci. Proc.*, 21, 347.
4. Yun, H.M. and DiCarlo, J.A. (2001) *Ceram. Eng. Sci. Proc.*, 22, in print.
5. Heredia, F.E., McNulty, J.C., Zok, F.W., and Evans, A.G. (1995) *J. Am. Ceram. Soc.*, 78, 2097.
6. Lipetzky, P., Stoloff, N.S., and Dvorak, G.J.,(1997) *Ceram. Eng. Sci. Proc.*, 18, 355.
7. Morscher, G.N., Gyekenyesi, J.Z., and Bhatt, R.T. (2000) In: *Mechanical, Thermal and Environmental Testing and Performance of Ceramic Composites and Components, ASTM STP 1392*, pp. 306-319. Jenkins, M.G., Lara-Curzio, E., and Gonczy, S.T. (Eds.), ASTM, West Conshohocken, PA.
8. Morscher, G.N. (1999) *Comp. Sci. Technol.*, 59, 687.
9. Morscher, G.N. (2000) *Review of Progress in Quantitative Nondestructive Evaluation*, Vol. 19A, pp. 383-390. Thompson, D.O. and Chimenti, D.E. (Eds.). American Institute of Physics, NY.
10. Eldridge, J.I., Bansal, N.P., and Bhatt, R.T. (1998) *Ceram. Eng. Sci. Proc.*, 19, 11.
11. Steen, M. and Valles, J-L. (1997) In: *Thermal and Mechanical Test Methods and Behavior of Continuous-Fiber Ceramic Composites, ASTM STP 1309*, pp. 49-65. Jenkins et al. (Eds.), ASTM, West Conshohocken, PA.
12. Domergue, J-M., Heredia, F.E., and Evans, A.G., (1996) *J. Am. Ceram. Soc.*, 70, 161.
13. Pluvinage, P., Parvizi-Majidi, A., and Chou, (1996) T.W., *J. Mater. Sci*, 31, 232.
14. Guilloumat, J. and Lamon, J. (1996) *Comp. Sci. Technology*, 56, 803.
15. Aveston, J., Cooper, G., and Kelly, A. (1971) *Proc. Natl. Phys. Lab.*, pp. 15-26. IPC Science and Technology Press, Surrey, U.K.
16. Budiansky, B., Hutchinson, J.W., and Evans, A.G. (1986) *J. Mech. Phys. Solids*, 34, 167.
17. Lissart, N. and Lamon, J., (1997) *Acta mater.*, 45, 1025.
18. Pryce, A.W. and Smith, P.A. (1993) *Acta metal. mater.*, 41, 1269.
19. Curtin, W.A., Ahn, B.K., and Takeda, N. (1998) *Acta mater.*, 46, 3409.
20. Ahn, B.K. and Curtin, W.A. (1997) *J. Mech. Phys. Solids*, 45, 177.